Eur. Phys. J. Plus (2017) **132**: 333
DOI 10.1140/epjp/i2017-11601-y

THE EUROPEAN PHYSICAL JOURNAL PLUS

Regular Article

Enhancement of piezoelectric properties for [poly (vinylidene fluoride)/barium zirconate titanate] nanocomposites

O.M. Hemeda[1], A. Tawfik[1], M.M. El-Shahawy[1,a], and K.A. Darwish[1,2]

[1] Physics Department, Faculty of Science, Tanta University, Tanta, Egypt
[2] Physics Department, Faculty of engineering, Modern academy for engineering and technology, Cairo, Egypt

Received: 15 January 2017 / Revised: 10 June 2017
Published online: 3 August 2017 –

Abstract. Poly (vinylidene fluoride) / barium zirconate titanate nanocomposite samples with the formula [x (PVDF) / $(1-x)$ BZT] (where x = zero, 0.2, 0.4, 0.6, 0.8 and 1) are prepared using the hot pressing method. The BZT is prepared using the tartrate precursor method. The properties of these nanocomposites are characterized by X-ray diffraction (XRD), scan electron microscope (SEM), transmission electron microscope (TEM) and Fourier transformed infrared (FTIR) at room temperature. The XRD patterns indicate that the average crystallite size ranges from 7.5 to 23.8 nm. The grain size is estimated from SEM micrograph and lies between 263 and 186 nm, whereas the average crystallite size has a distribution between 14 and 70 nm from TEM images. The FTIR spectra illustrate the absence of any absorption band related to the (γ) phase, but the absorption bands characteristic for (α), and (β) phases of PVDF are observed. The fraction of the (β) phase of PVDF increases by increasing the BZT content, which is very useful in industrial applications, such as sensors, actuators and transducers. The high value of the piezoelectric coefficient d_{33} is measured for the PVDF/BZT nanocomposites.

1 Introduction

In the last few decades, many researchers have studied new materials that have high dielectric permittivity and good mechanical properties for important technological applications. Ferroelectric ceramics have much higher dielectric values than polymers but with poor mechanical properties and a lower dielectric breakdown strength. On the other hand, polymers are characterized by their flexibility, and they have a high strength of dielectric breakdown [1–3].

Polymer/ceramic nanocomposite materials have a wide range of applications because of their improved individual constituent properties. A composite with high dielectric permittivity and high breakdown strength could be developed by integrating high dielectric permittivity ceramic, as BZT nanoparticles, with the PVDF polymer [4,5].

At present, many polymers, such as PVDF, polyethylene, and polystyrene can be used as dielectrics in capacitors due to their large electric breakdown. PVDF represents one of the most important polymers because of its chemical stability, high elasticity modulus, and very high piezoelectric response compared with other polymers, which makes it useful in the fabrication of actuators and sensors. In addition, PVDF is the most selected material to be used as a dielectric, due to its high dielectric strength and permittivity, and low dissipation factor [6–8].

Ferroelectric materials are used in the fabrication of various devices, such as transducers, capacitors, actuators, sensors, etc., and they are widely used in many electronic components. Barium zirconate titanate (BZT) has gained great importance because of its high permittivity, high dielectric constant, low dielectric loss, and large tunability, because Zr^{4+} is chemically more stable than Ti^{4+}. The stability of Zr^{4+} leads the composite to be better suited for several advanced applications, such as microwave technology and piezoelectric devices [9–11].

Recently, various physical and chemical techniques are used to prepare nanomaterials. The widely used chemical methods are co-precipitation [12], hydrothermal [13,14], reverse micro-emulsion [15,16], auto combustion method [17], citrate Sol-Gel technique [18,19] and tartaric acid precursor technique [20,21].

Among these techniques, the tartaric acid precursor technique involves the preparation of an aqueous solution of the required cation. The chelation of cations in solution is caused by addition of tartaric acid, then the temperature of the solution is increased until formation of the precursor. The precursor is calcined at low temperatures, compared with other methods, to form the ferroelectric nanopowder. This method is very simple, cheap and available for most of piezoelectric materials [20,21].

[a] e-mail: Mohammed_Elshahawy@science.tanta.edu.eg (corresponding author)

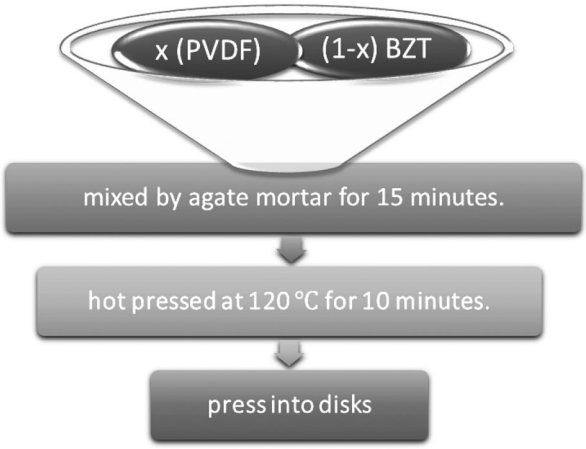

Fig. 1. The flowchart for the hot press method.

The present study aims to enhance the piezoelectric properties of a [poly (vinylidene fluoride) /barium zirconate titanate] nanocomposite. The hot press method helps the constituents to be homogenously distributed. The obtained (PVDF/BZT) nanoparticles were characterized by XRD, SEM, TEM and FTIR spectra.

2 Experiment

2.1 Materials

All chemicals used in this work, including barium nitrate $Ba(NO_3)_2$, titanium dioxide TiO_2, zirconium oxide ZrO, tartaric acid $C_4H_6O_6$ are of analytical grade. The poly (vinylidine fluoride) (PVDF) $(–CH_2–CF_2–)_n$ with average molecular weight 534000 is purchased from Sigma-Aldrich®.

2.2 Synthesis of BZT nanoparticles

The tartrate precursor method is used for the preparation of BZT nanoparticles. The mixtures of 0.1 mole of [$Ba(NO_3)_2$, ZrO, TiO_2] and 0.3 moles of tartaric acid solutions are prepared, then 250 mL distilled water is added and stirred for 15 minutes on a hot plate magnetic stirrer. The temperature is raised to 80 °C with constant stirring until dryness of the solution. The precipitation is dried in a dryer at 200 °C for 24 hours. The resulting material is hand-grinded in air using an agate mortar to obtain homogeneous BZT nanoparticles.

2.3 Preparation of PVDF/BZT nanocomposites

The nanocomposite polymer [x (PVDF) / $(1-x)$ BZT] samples (where x= zero, 0.2, 0.4, 0.6, 0.8 and 1) are prepared using the hot pressing method. The mass percentage of x (PVDF) is added to $(1-x)$ BZT in grams and then grinded using an agate mortar for 15 minutes. For fabrication, the composite is hot pressed as disks at 120 °C for 10 minutes with a pressure of 5 tons as shown in fig. 1.

2.4 Characterization of PVDF/BZT nanocomposites

The X-ray diffraction (XRD) of nanocomposites is carried out at room temperature using the APD 2000 pro, H423-virtical diffractometer, equipped with Cu Kα radiation (λ = 1.540598 Å). The grain size and the samples surface morphology are obtained by Quanta FEG-250 Scanning Electron microscope (SEM). The particle size of nanocomposites is investigated by JEOL JEM-2100 transmission electron microscope (TEM). The TEM specimen is prepared by the ultrasonic dispersion of a small amount of powders in a few milliliters of ethanol, and is then dropped on a copper grid covered by an amorphous carbon film. Fourier transformed infrared spectroscopy (FTIR) spectra analysis is carried out at room temperature using a BRUKER FT-IR spectrometer tensor 27 in the range of 200 to 4000 cm^{-1}.

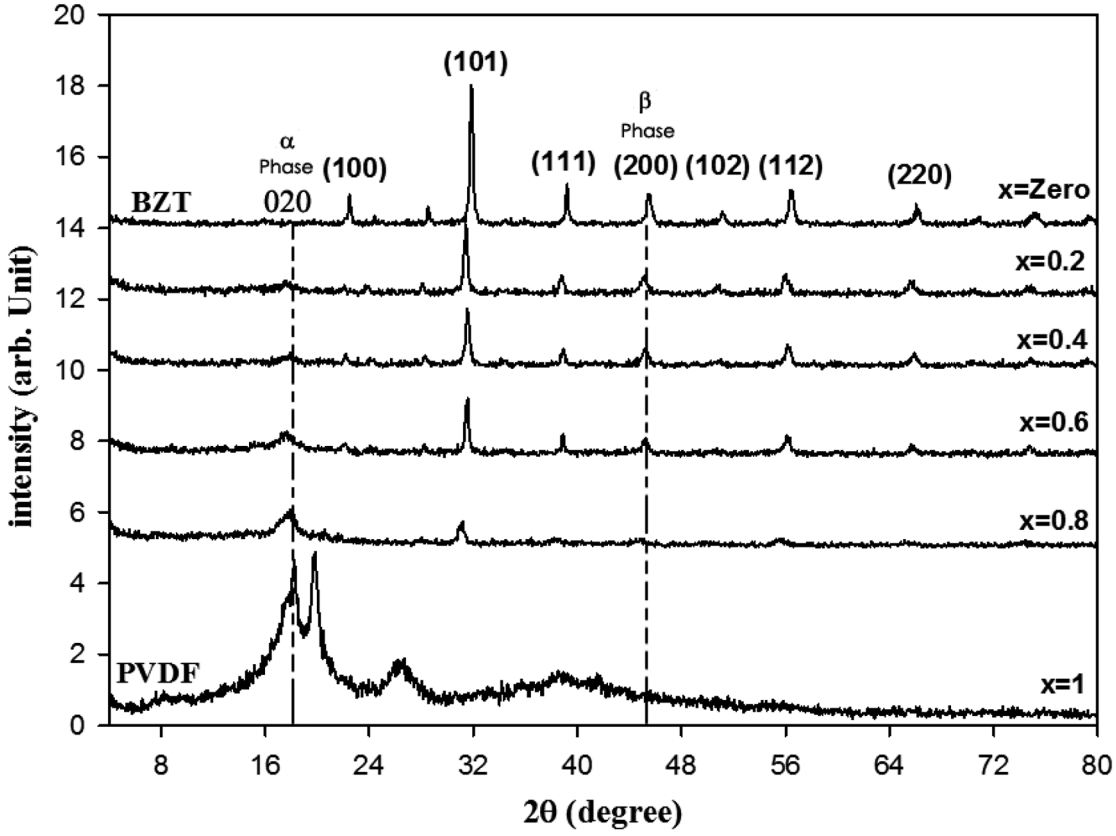

Fig. 2. The XRD patterns of the prepared [x (PVDF) / $(1-x)$ BZT] nanocomposites (where x= zero, 0.2, 0.4, 0.6, 0.8 and 1).

3 Results and discussion

3.1 X-Ray diffraction studies

Figure 2 shows the XRD patterns of the prepared [x (PVDF) / $(1-x)$ BZT] nanocomposites (where x= zero, 0.2, 0.4, 0.6, 0.8 and 1). The XRD patterns show a typical perovskite structure without any foreign secondary phase peaks. The PVDF shows a semi-crystalline structure with some peaks which belong to the unpolarized (α) phase and others belonging to the polarized (β) phase. The ferroelectric phase is still dominating the crystal properties of the composite up to $x = 0.4$. The reflected peaks reveal the formation of a stable solid-state solution composite from BZT and PVDF, since no extra peaks appear in the XRD pattern [22].

To investigate the inference of ferroelectric polymer PVDF on ferroelectric ceramic BZT, XRD studies are performed for pure PVDF and BZT based ferroelectric ceramic. High peaks are caused by the (020) and (021) crystal planes at $2\theta \cong (18.6, 27°)$. The peaks belong to the (α) phase of PVDF, while those caused by the plane (200) at $2\theta \cong (45.4°)$ belong to the (β) phase of PVDF [23–25]. It is noticed from the XRD patterns that the (α) phase content decreases by increasing the BZT ratio, which means that the (α) phase is transferred to the (β) phase by addition of BZT. This is a very important notification in industry, because the (β) phase represents a piezoelectric phase due to its polar character.

The structural parameters of (PVDF/BZT) nanocomposites including lattice parameters, a and c, cell volume, V, and the crystallite size, D, are given in table 1. The average crystallite size (D) is calculated using the Scherer's equation as follows:

$$D = 0.9\frac{\lambda}{h_{1/2}\cos\theta_B}\,, \tag{1}$$

where λ is the wavelength for Cu-Kα ($\lambda = 1.540598\,$Å), $h_{1/2}$ is the full width at half maximum (FWHM) of the diffraction peak in radian, and θ_B is the diffraction angle.

As is shown in the table, the average crystalline size of the samples prepared by the tartaric acid method lies in the nanometer range (7.5–23.8 nm).

Table 1. The structural parameters of (PVDF/BZT) nanocomposites.

x	Lattice parameters		c/a	Crystallite size	Cell volume
	a (Å)	c (Å)		D (nm)	V (Å)^3
0	3.9868	4.0061	1.0048	23.77	63.68
0.2	4.0170	4.0240	1.0017	18.59	64.93
0.4	4.0177	4.0251	1.0016	16.98	64.97
0.6	4.0042	4.0060	1.0005	16.66	64.23
0.8	4.0396	4.0680	1.0070	7.50	66.38

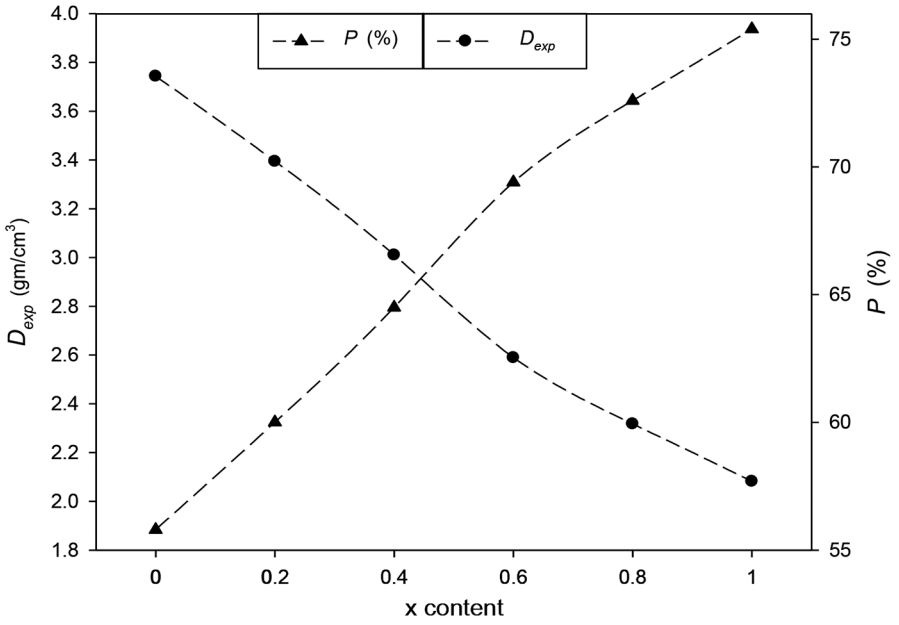

Fig. 3. The bulk density $D_{\exp}$ and the porosity P of the composite samples *vs.* the PVDF content.

Figure 3 shows the bulk density ($D_{\exp}$) and the porosity (P) of the composite samples *vs.* PVDF content. The porosity is increased by increasing the PVDF content, due to the increase of the intergranular pores as a result of the PVDF addition. On the contrary, the bulk density decreases by increasing the PVDF content.

3.2 The scanning electron microscope (SEM)

The SEM micrographs for all nanocomposite samples are shown in fig. 4. As is shown from the SEM of the samples, the PVDF samples surround the BZT grains, leading to a decrease in its grain size by increasing the PVDF content. The grain size estimated from SEM micrograph lies between 263 and 186 nm. Moreover, the SEM micrograph of PVDF exhibits no features, due to the absence of any crystalline morphology. The microstructure of the PVDF/BZT composite illustrated by SEM clearly indicates the presence of BZT grains as a bright dense roughness region, while the dark region is related to the PVDF polymer with smooth surface. In addition, the figures show that the BZT is homogenously dispersed in the PVDF polymer matrix. Our results are confirmed by previous results [1]. It is noticed that the homogenous distribution increases by decreasing the PVDF content and the increase in the particle size [26].

3.3 The transmission electron microscope (TEM)

The transmission electron microscope (TEM) images of the PVDF/BZT nanocomposites are shown in fig. 5. It is found that the nanocomposite samples consist of particles having distribution between 14 and 70 nm. Although the XRD is a useful tool for determining the crystal size, it does not give information about its size distribution. On the other hand, the TEM can be used to give information about the shape and size distribution of the nanoparticles.

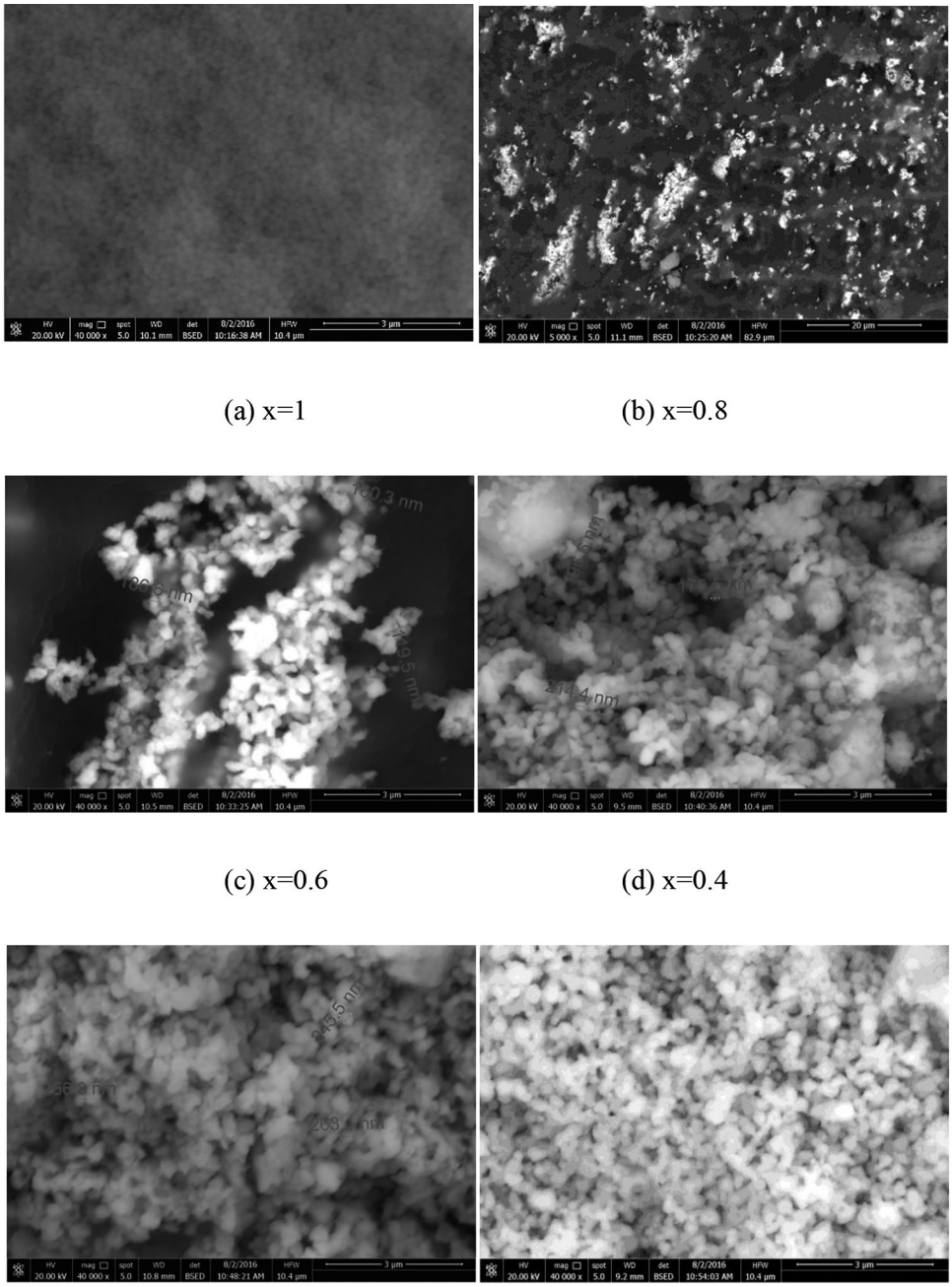

Fig. 4. The SEM micrograph [x (PVDF) / $(1-x)$ BZT] nanocomposites.

The PVDF micrograph shows a spherical particle in an agglomerated state. However, the TEM micrograph shows that the BZT crystallite dark region is surrounded by a PVDF bright region and it forms what is called a core shell, which is very important in many industrial applications, such as sensors, actuators and transducers [27]. A stable and dense polymer shell clearly coated the surface of BZT nanoparticles. The thickness of the coating polymer shell is about 8–9 nm [28]. The tetragonality character of the BZT crystallite is illustrated in the BZT sample. It can be noticed, from the TEM micrograph, that the crystallite size decreases by increasing the PVDF content. The core shell phenomenon is the reason for this behavior, because the accumulation of PVDF polymer around the BZT nanoparticles retards the crystallite growth, leading to a decrease in its size. The same result is obtained from the analysis of the XRD pattern using Scherer's equation. The crystallite size obtained from XRD and particle size obtained from TEM micrograph are given in table 2.

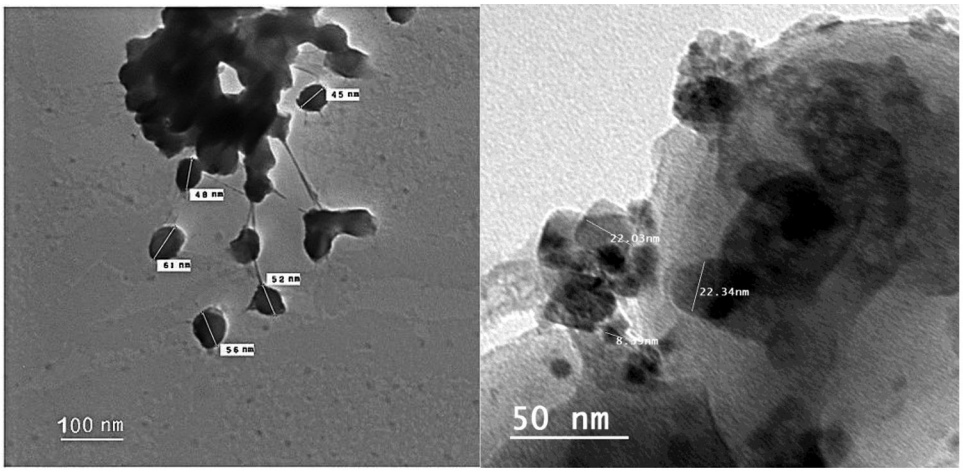

(a) x=1 (b) x=0.8

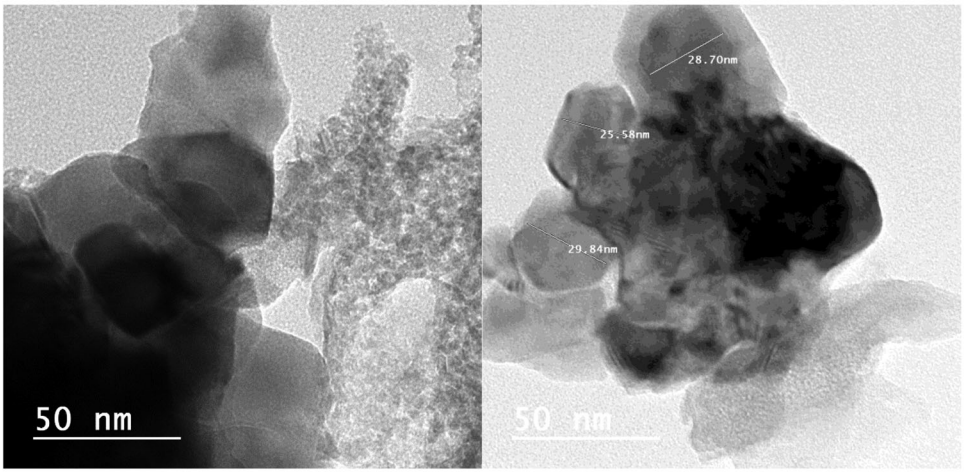

(c) x=0.6 (d) x=0.4

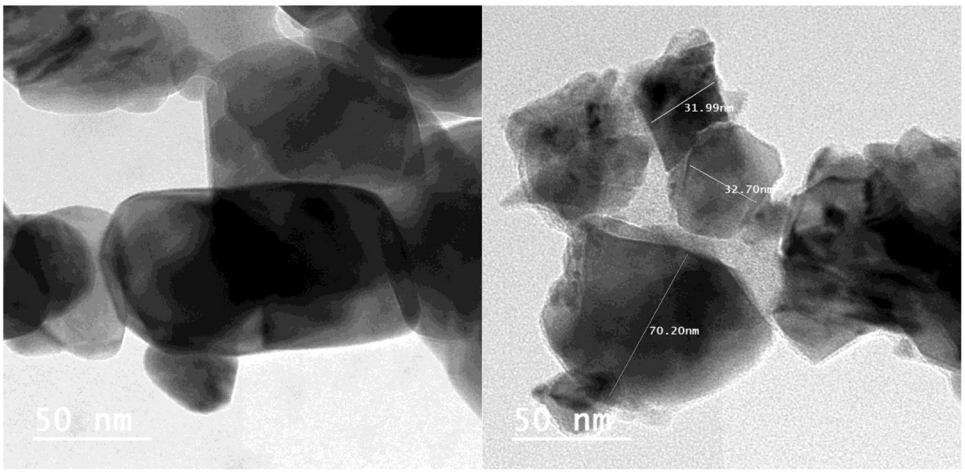

(e) x=0.2 (f) x=zero

Fig. 5. The TEM micrograph of [x (PVDF) / $(1-x)$ BZT] nanocomposites.

Table 2. The crystallite size from XRD and particle size from TEM micrograph with x content.

x content	Crystallite size from XRD (nm)	Crystallite size from TEM (nm)	Grain size from SEM (nm)
0	24	39	258
0.2	21	32	246
0.4	19	28	176
0.6	17	18	120
0.8	8	10	111

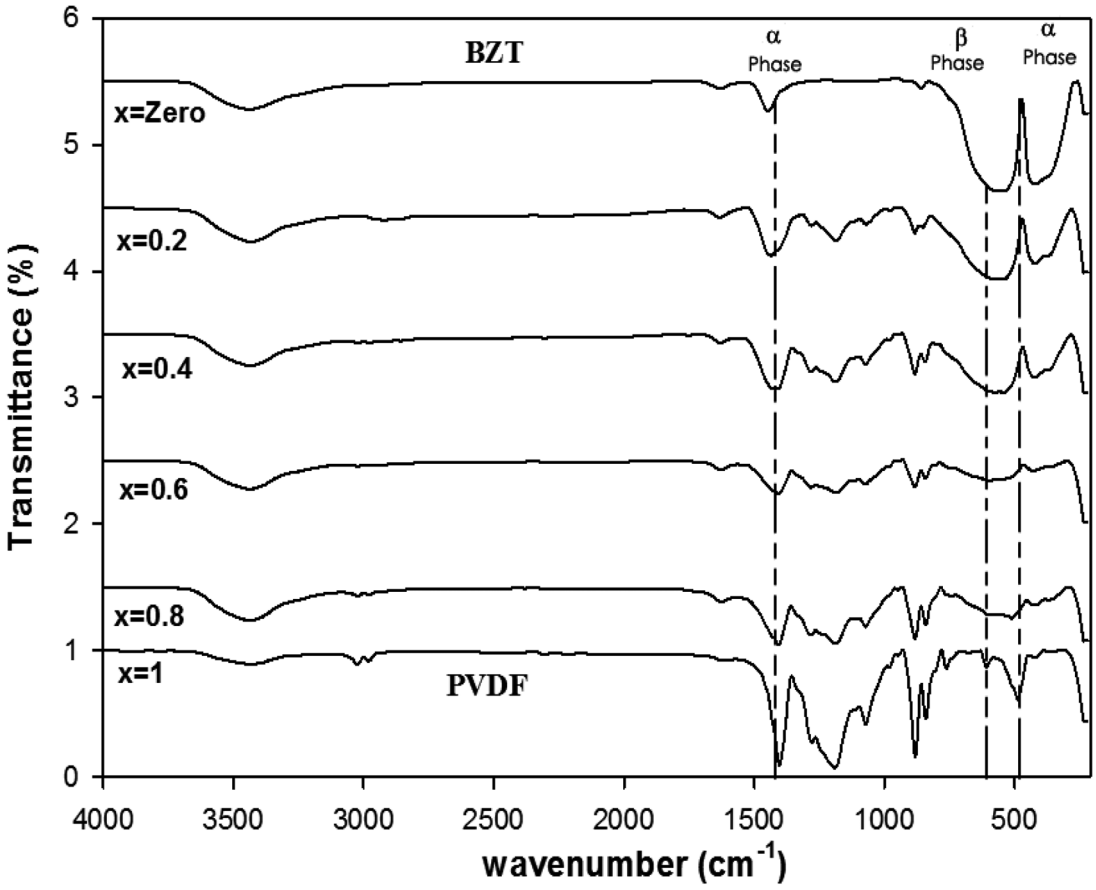

Fig. 6. FTIR of the PVDF/BZT nanocomposite samples.

3.4 The Fourier transformed infrared (FTIR)

The FTIR spectra at room temperature in the range of 200–4000 cm^{-1} for the PVDF/BZT nanocomposite samples are shown in fig. 6.

The absorption spectra provide rich information about the different phase transformation, which occurred in PVDF due to the addition of BZT. It is well known that the formation of PVDF consists of different phases according to the arrangement of fluorine ions, carbon and hydrogen atoms. The (α) and (γ) phases are non-polar, whereas the (β) phase is polar due to the regular arrangement of negative fluorine on one side of the chain and of the positive hydrogen ion on the other side. PVDF as a raw material shows predominantly the (α) phase (non-polar phase), while the presence of the (β) phase is enhanced by different methods. It is preferable to transfer the (α) phase to the (β) phase by annealing either at high temperature or high pressure.

Table 3. The absorption FTIR bands characteristics of the (α) and (β) phase-PVDF.

	α	β
Wave number (cm^{-1})	481-615-766-880-979-1185-1403	426-532-840-1287

Table 4. The fraction of the (β) phase of PVDF with PVDF content.

PVDF content	BZT content	F (β)
1	0.00	0.466
0.8	0.2	0.473
0.6	0.4	0.487
0.4	0.6	0.494
0.2	0.8	0.497

The FTIR spectra show that the absorption bands at 426, 532, 840 and 1287 cm^{-1} are related to the (β) phase. The bands at 1287 and 532 cm^{-1} are assigned to C-H_2 and C-F_2 bending vibration bands, respectively, where 426 cm^{-1} is a stretching vibration, which is parallel to the a-axis of the PVDF chain [27]. The (α) phase is observed at 481, 615, 766, 880, 979, 1185, and 1403 cm^{-1}. The absorption band appears at 1403 cm^{-1} attributed to C-H_2 wagging vibration, but the C–C band of PVDF is observed at 1185 cm^{-1}. The band at 880 cm^{-1} is related to the C–C–C asymmetrical stretching vibration of PVDF, while that at 766 cm^{-1} is related to the vibration of the PVDF chain. The band at 615 cm^{-1} belongs to the bending vibration of C-F_2, where the bending and waging vibrational frequency is observed at 481 cm^{-1}, which is the characteristic absorption band for the (α) PVDF phase [23,25,29]. Our FTIR results illustrate the absence of any absorption band related to the (γ) phase, as summarized in table 3.

The fraction of (β) phase was calculated by using the following equation [30,31]:

$$F(\beta) = A_\beta/[1.26(A_\alpha) + A_\beta], \tag{2}$$

where A_α and A_β are the absorption band intensity for the (α) and (β) phases, respectively.

This fraction found to increase by increasing the BZT content as shown in table 4, which is useful in industry applications and is considered as a simple tool to obtain a polar piezoelectric PVDF.

These results are in agreement with the result of XRD diffraction for our nanocomposites. It is found that the broad absorption band at 3420 cm^{-1} frequency is attributed to the stretching vibration of the O-H group. The absorption bands at 541 and 421 cm^{-1} for pure BZT are assigned to the stretching vibration of the BaO_2 and TiO_2 bond, respectively.

3.5 Piezoelectric modulus (d_{33}) of the nanocomposite samples

The effect of PVDF on the piezoelectric modulus (d_{33}) of the nanocomposite samples is shown in fig. 7. It is noticed that (d_{33}) increases gradually as BZT content increases; this can be explained as follows.

The micro structural study shows that the grain size is increased by increasing BZT, *i.e.*, the decrease in the grain size decreases the volume fraction of the grain boundary. Therefore, increasing the domain wall mobility under the applied stress increases the (d_{33}) modulus by increasing BZT. The orientation of the molecular chain and self-align dipoles enhance the piezoelectric response, and are observed during the addition of BZT. The d_{33} of our composite is the result of the linear relationship between the applied stress and the generated piezoelectric charge. The dependence of d_{33} on BZT content is shown in fig. 7, which illustrates that the d_{33} increases by increasing the BZT content due to the transformation of the (α) non-polar phase to the (β) polar phase. This transformation is confirmed by the XRD and IR spectra. The most advantage result of our work is obtaining the polar phase of PVDF only by the addition of BZT content instead of other methods. Drawing and annealing under different pressure conditions are examples for phase transfer. The phase transfer methods are shown in fig. 8. The increase of d_{33} is due to the increase of BZT ions, which leads to more ionic displacement under the applied mechanical stress.

A correlation between the DC conductivity and the piezoelectric effect can be estimated from fig. 9. At low BZT concentration, the conduction mechanism is due to the insulating PVDF, which slowly increases the d_{33} value by increasing BZT as shown in fig. 7 [32]. The transformation from the (α) to the (β) phase leads to the change of the conduction mechanism from insulating to ionic and bipolar conduction mechanisms and, consequently, the d_{33} increases sharply.

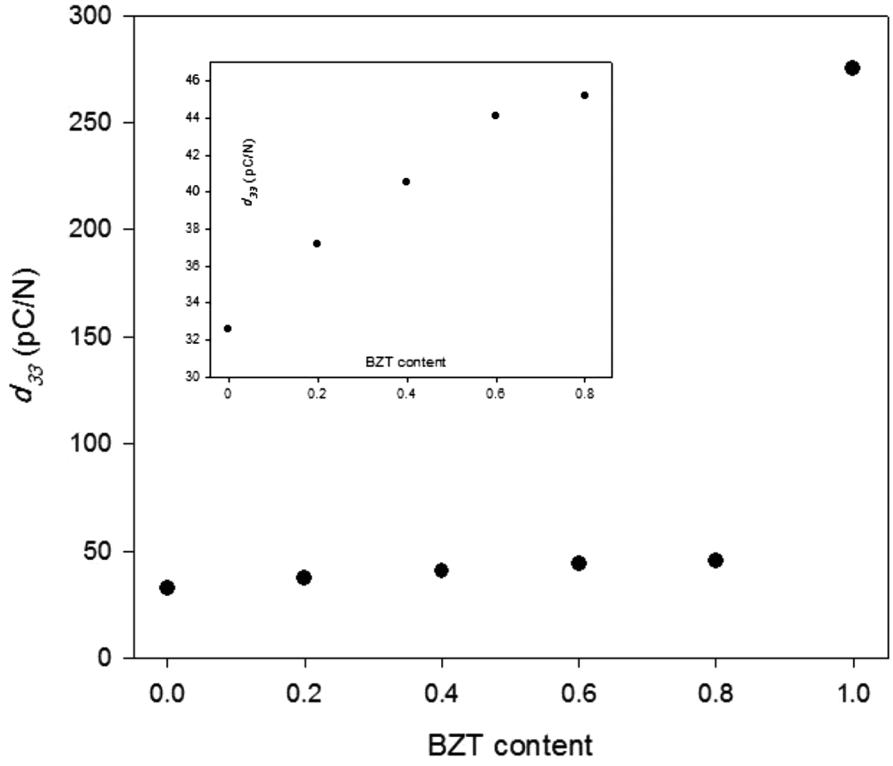

Fig. 7. The piezoelectric modulus (d_{33}) of the BZT content.

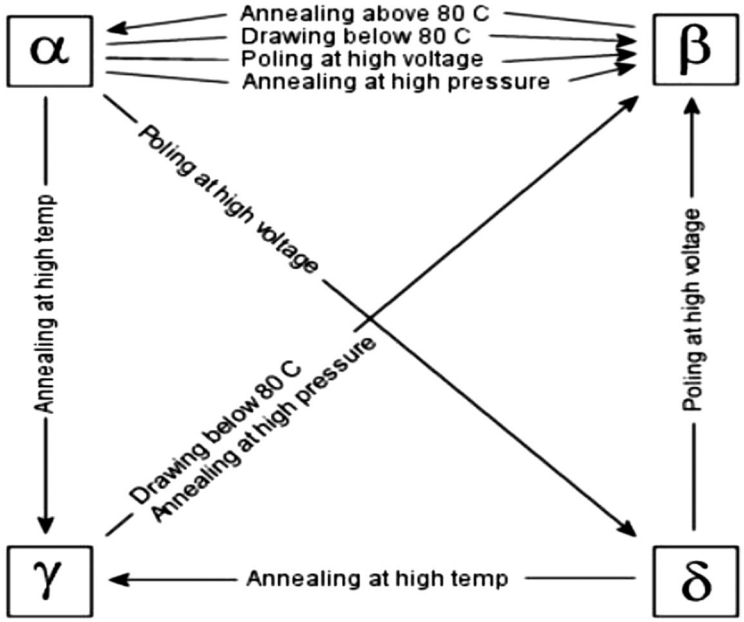

Fig. 8. The diagram shows how each of the crystalline phases of PVDF can be achieved.

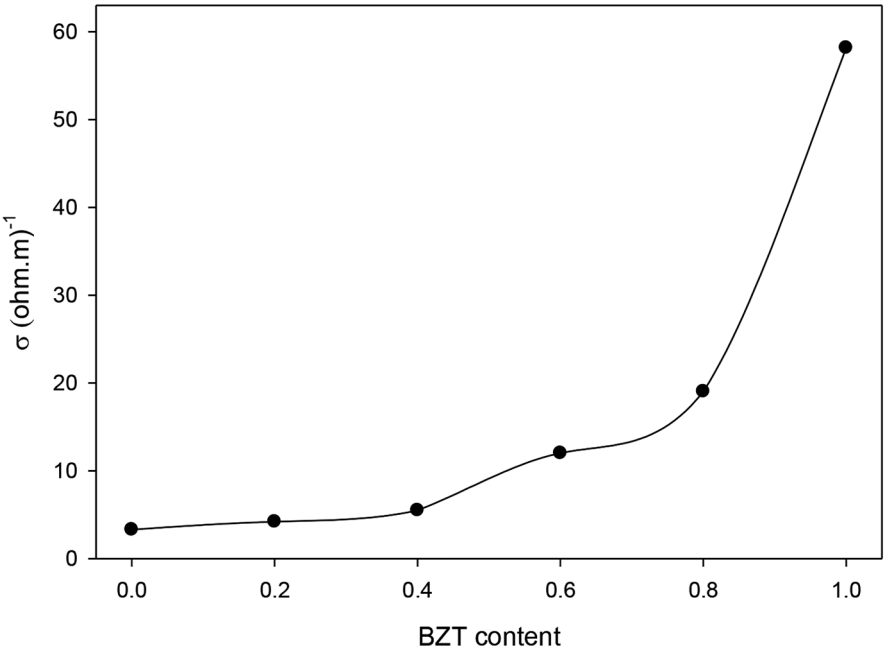

Fig. 9. The dc conductivity σ of the BZT content.

Table 5. Results of d_{33} for our composite and published data for PVDF composite, where BCT is barium carbonate titanate, CCTO is calcium cupper titanate and TrFE is trifluoroethylene.

Composition	d_{33} (pC/N)	Reference
0.25(BZT-BCT)−0.75(PVDF)	−31	[33]
0.25(BZT-BCT)−0.75(0.2 PVDF- 0.8 CCTO)	−19	[33]
(PVDF-TrFE)	−38	[34]
PVDF	−33	[35]
0.8(BZT)+0.2(PVDF)	−45	Present work

Table 5 indicates the result of d_{33} for our composite and published data for PVDF composite. The piezoelectric constant is negative, which means that when the electric field is applied in the same direction of the polarization, the thickness of the composite sample decreases.

4 Conclusions

The ferroelectric nanoparticles of BZT are synthesized by the tartrate precursor method and [x (PVDF) / $(1-x)$ BZT] nanocomposites (where x= zero, 0.2, 0.4, 0.6, 0.8 and 1) are prepared using the hot pressing method. The XRD patterns show a typical perovskite structure without any foreign secondary phase. SEM micrograph shows the homogeneous distribution of the ceramic in the polymer. The TEM micrograph shows the BZT crystallite as a dark regions surrounded by bright PVDF regions to form a core shell, which is very important in many industrial applications, such as sensors, actuators and transducers. The fraction of the (β) phase is calculated from FTIR spectra and is found to increase by increasing the BZT content. The piezoelectric modulus (d_{33}) is found to increase by increasing the BZT content, which enhances the piezoelectric properties of (PVDF) nanoparticles.

References

1. T. Badapanda, V. Senthil, S. Anwar, L. Cavalcante, N. Batista, E. Longo, Curr. Appl. Phys. **13**, 1490 (2013).
2. Y. Song, Y. Shen, H. Liu, Y. Lin, M. Li, C.-W. Nan, J. Mater. Chem. **22**, 8063 (2012).
3. M.T. Sebastian, H. Jantunen, Int. J. Appl. Ceram. Technol. **7**, 415 (2010).
4. V. Senthil, T. Badapanda, A. Chithambararaj, A.C. Bose, A. Mohapatra, S. Panigrahi, J. Polym. Res. **19**, 1 (2012).
5. K. Li, G. Pang, H.L.W. Chan, C.L. Choy, J.-h. Li, J. Appl. Phys. **95**, 5691 (2004).
6. S. Adireddy, V.S. Puli, T.J. Lou, R. Elupula, S. Sklare, B.C. Riggs, D.B. Chrisey, J. Sol-Gel Sci. Technol. **73**, 641 (2015).
7. Y. Wang, X. Zhou, Q. Chen, B. Chu, Q. Zhang, IEEE Trans. Dielectr. Electr. Insul. **17**, 1036 (2010).
8. D.M. Esterly, *Manufacturing of Poly (vinylidene fluoride) and Evaluation of its Mechanical Properties* (2002).
9. U. Weber, G. Greuel, U. Boettger, S. Weber, D. Hennings, R. Waser, J. Am. Ceram. Soc. **84**, 759 (2001).
10. X. Tang, J. Wang, X. Wang, H. Chan, Solid State Commun. **131**, 163 (2004).
11. Z. Yu, C. Ang, R. Guo, A. Bhalla, J. Appl. Phys. **92**, 1489 (2002).
12. P. Seeharaj, S. Wirunchit, P. Charoonsuk, P. Kim-Lohsoontorn, N. Vittayakorn, Ferroelectrics **455**, 83 (2013).
13. H. Takahashi, Y. Numamoto, J. Tani, S. Tsurekawa, Jpn. J. Appl. Phys. **45**, 7405 (2006).
14. X. Zhu, Z. Zhang, J. Zhu, S. Zhou, Z. Liu, J. Cryst. Growth **311**, 2437 (2009).
15. M.R. Varma, S. Biju, M. Sebastian, J. Eur. Ceram. Soc. **26**, 1903 (2006).
16. C.-H. Lu, S.-Y. Chen, C.-H. Hsu, Mater. Sci. Eng.: B **140**, 218 (2007).
17. G.K. Sahoo, R. Mazumder, J. Mater. Sci.: Mater. Electron. **25**, 3515 (2014).
18. Z.-m. Wang, K. Zhao, X.-l. Guo, W. Sun, H.-l. Jiang, X.-q. Han, X.-t. Tao, Z.-x. Cheng, H.-y. Zhao, H. Kimura, J. Mater. Chem. C **1**, 522 (2013).
19. M. Wang, R. Zuo, S. Qi, L. Liu, J. Mater. Sci.: Mater. Electron. **23**, 753 (2012).
20. M. Hessien, Int. J. Appl. Nat. Sci. **2**, 9 (2013).
21. M. Hessien, N. El-Bagoury, M. Mahmoud, O.M. Hemeda, High Temp. Mater. Processes **35**, 499 (2016).
22. P. Mishra, P. Kumar, Adv. Condens. Matter Phys. **2013**, 858406 (2013).
23. P. Martins, A. Lopes, S. Lanceros-Mendez, Prog. Polym. Sci. **39**, 683 (2014).
24. P. Martins, C.M. Costa, G. Botelho, S. Lanceros-Mendez, J. Barandiaran, J. Gutierrez, Mater. Chem. Phys. **131**, 698 (2012).
25. H. Bai, X. Wang, Y. Zhou, L. Zhang, Prog. Nat. Sci.: Mater. Int. **22**, 250 (2012).
26. V. Senthil, T. Badapanda, S. Kumar, P. Kumar, S. Panigrahi, J. Polym. Res. **19**, 1 (2012).
27. A. Zak, W. Gan, W.A. Majid, M. Darroudi, T. Velayutham, Ceram. Int. **37**, 1653 (2011).
28. Y. Qiao, M.S. Islam, L. Wang, Y. Yan, J. Zhang, B.C. Benicewicz, H.J. Ploehn, C. Tang, Chem. Mater. **26**, 5319 (2014).
29. R. Simoes, M. Rodriguez-Perez, J. de Saja, C. Constantino, J. Therm. Anal. Calorim. **99**, 621 (2009).
30. R. Gonçalves, P. Martins, D.M. Correia, V. Sencadas, J. Vilas, L. León, G. Botelho, S. Lanceros-Méndez, RSC Adv. **5**, 35852 (2015).
31. M. Silva, G. Botelho, J. Rocha, S. Lanceros-Mendez, Polym. Testing **29**, 613 (2010).
32. T. Furukawa, Phase Transit. **18**, 143 (1989).
33. P. Kumar, *Lead-Free Ceramic-Polymer Composites for Embedded Capacitor and Piezoelectric Applications* (2015).
34. K. Omote, H. Ohigashi, K. Koga, J. Appl. Phys. **81**, 2760 (1997).
35. E. Nix, I. Ward, Ferroelectrics **67**, 137 (1986).